

Investigating the ability of deep learning to predict Welding Depth and Pore Volume in Hairpin Welding

Amena Darwish*, Stefan Ericson, Rohollah Ghasemi, Tobias Andersson, Dan Lönn, Andreas Andersson Lassila, Kent Salomonsson

Virtual Manufacturing Processes, School of Engineering Sciences, University of Skövde,
Kaplangatan 11, Skövde 54134, Sweden

*Corresponding author: amena.darwish@his.se

Abstract

To advance quality assurance in the welding process, this study presents a deep learning DL model that enables the prediction of two critical welds' Key Performance Characteristics (KPCs): welding depth and average pore volume. In the proposed approach, a comprehensive range of laser welding Key Input Characteristics (KICs) is utilized, including welding beam geometries, welding feed rates, path repetitions for weld beam geometries, and bright light weld ratios for all paths, all of which were obtained from hairpin welding experiments. Two DL networks are employed with multiple hidden dense layers and linear activation functions to showcase the capabilities of deep neural networks in capturing the complex nonlinear relationships between the welding input and output variables (KPCs and KICs).

Applying DL networks to the small numerical experimental hairpin welding dataset has shown promising results, achieving Mean Absolute Error (MAE) values 0.1079 for predicting welding depth and 0.0641 for average pore volume. This, in turn, promises significant advantages in controlling welding outcomes, moving beyond the current trend of relying only on defect classification in weld monitoring, to capture the correlation between the weld parameters and weld geometries.

Keywords: Data-driven analytics, Deep learning, Hairpin welding, Quality assurance of laser welding, Welding similar materials.

1 Introduction

Climate change is a serious global challenge, and the European Union's 2030 Climate Target Plan aims to substantially reduce at least 55% of greenhouse gas emissions compared to 1990 levels by 2030 [1]. Meeting the European Union's emission reduction goals heavily relies on electric powertrains. The key component in these powertrains is the electric motor, which needs to be highly efficient and high-performing. This requires the winding and joining of the copper wires to the motor parts to increase the power density. However, a major challenge lies in the winding process, which causes significant power losses [2]. Traditional winding and joining technologies face strict limitations in terms of accessibility and potential damage to the insulating layer [3]. Therefore, adopting innovative technologies that can minimize power losses caused by the winding and joining process is essential. One effective approach is hairpin winding, which involves windings comprising robust U-shaped insulated copper conductors with rectangular cross-sections [4]. However, this approach requires multiple bending and welding points to ensure the electrical circuit of the hairpin winding [5].

Laser beam welding (LBW) is commonly recommended as a viable solution for hairpin winding due to its non-physical contact nature, high-speed beam, exceptional precision, energy density, automation capabilities, and superior weld quality [6], [7]. Moreover, laser welding shows a high degree of versatility as it can be employed across a wide range of materials, including metals, alloys [1], and non-metallic materials [8]. This characteristic of versatility renders it widely applicable in different sectors, such as automotive [9], aerospace [10], medical device manufacturing [11], and other industrial applications [12].

Despite its unique advantages, laser welding is a complex manufacturing process due to its high energy density; the interaction between the laser beam and, in this case, the metal parent material is characterized by a strong metal melting and solidification result. Consequently, apart from the laser process parameters such as welding speed and path, laser power, focused position, and the welding conditions, such as the microstructure of the parent materials and the cleanliness of the workpiece surfaces, significantly impact the quality of the achieved welds. Additionally, the physical phenomena of melting and solidifying metal (keyhole formation, molten pool behavior, spatter, and plasma plume should be considered [7]. Thus, there is a demand for in-situ laser monitoring approaches/methodologies. To clarify the term 'monitoring' within this paper, it extends beyond mere observation; instead, it involves data collection, laser process identification and modeling, and defect detection based on pre-analyzed rules [13].

The welding's key factors in the literature are classified into three types for a solid understanding as follows:

- (1) The pre-processing stage includes the laser beam parameters (key input characteristics KICs). It is divided into changeable parameters (laser energy, geometry of the beam path, speed of the laser beam) and predefined parameters (the material properties, material thickness, workpiece conditions, and laser type). All KICs are set up before the welding process is started.
- (2) The stage of in-process monitoring is dedicated to observing the welding zone, including Key Measurement Characteristics (KMCs). It is about the physical phenomenon of melting and solidifying metal (keyhole formation, molten pool behavior, spatter, and plasma plume).
- (3) Post-processing involves detecting and evaluating sample defects (pores, cracks, and keyhole collapse), and it is called KPCs (Key Performance Characteristics) [14]. The primary challenge in an in-situ monitoring case relates to the precise prediction and identification of the final welding characteristics of KPCs within a dynamic and nonlinear process distinguished by many interrelated factors, including KMCs and KICs.

KPCs predictions rely significantly on computationally intensive multi-physics numerical simulations [15-22], making them inherently challenging and complex to solve. Nevertheless, an alternative approach is available by utilizing machine learning (ML) techniques. ML reduces the need for a deep understanding of the LBW process while still extracting significant insights from measurable data. Several studies [26, 27] demonstrated the utilization of real-time sub-monitoring systems, aiming to observe one or more KICs/KMCs during the welding processes to obtain one or more KPCs by applying classical ML or DL networks. The necessity for this investigation arises from a gap in the literature, where predicting weld geometries and weld defects using ML from non-image data is not a focal point in research. To highlight this gap, this study divides the literature into two types: first, utilizing ML to monitor/control the KPCs with non-image data, and second, applying DL on image datasets to predict one or more KPCs.

Yusof et al. [26] proposed a DL model that utilizes a conventional Artificial Neural Network (ANN) incorporating laser peak power and pulse duration variation as the two KICs. Furthermore, Yusof et al.'s model includes features derived from the acoustic emission sensor, specifically statistical features extracted from a sound signal. The model developed in Yusof et al.'s study demonstrated high accuracy in predicting the weld depth; it was trained using a dataset consisting of 195 samples. As outlined in Liu et al.'s model [27], they utilized a hybrid

methodology that combined the ANN with a genetic algorithm (GA) to predict both the number and average area of the porosities. In their model, the inputs consist of four KICs variables: laser power, welding speed, focal position, and beam separation. Liu et al.'s model exhibited commendable accuracy and effectively reduced the occurrence of porosities in welding 316L stainless steel. Adding to the presented works, Luo and Shin [28] proposed a ML model for keyhole geometry formation in the laser welding process of Stainless steel 304. Their model used a radial basis function neural network that takes four KICs (laser power, welding speed, focal diameter, and approximate keyhole diameter) to predict the keyhole features (considering the penetration depth and inclination angle).

DL has shown more ability to capture complex attributes from the data, which could result in improved accuracy in classifying welding processes in comparison to the traditional method of manual feature engineering. Researchers are increasingly adopting DL techniques, mainly conventional neural networks (CNNs), to analyze raw monitoring data from laser beam welding image datasets [29 - 33]. For instance, in Mayr et al.'s study [29], CNNs were applied to classify two-dimensional (2D) images obtained using a high-speed camera during hairpin welding. The classification process was conducted in both the pre-process and post-process stages, utilizing a dataset of about 500 images. The classification results demonstrated a high level of accuracy.

Similarly, in Zhao et al.'s model [30], an image processing technique was employed to examine various factors such as the coefficient of variation of vapor plume area (VPA), vapor plume orientation (VPO), and their correlation with the high-temperature zone (HTZ) of the molten pool that contains the keyhole, as well as the stability of the keyhole. In a study conducted by Hartung et al. [31], a novel approach was taken to develop a stacked dilated U-Net for in-process monitoring by adapting a vanilla U-Net model. They utilized high-speed camera imagery during the hairpin welding process to perform pixel-wise segmentation and accurately identify the spatter region. Shin et al. [32] used a DL model with CCD camera images as input to identify solidification cracks in AI 6000 alloy. Their model achieved 99.31% accuracy in prediction. Additionally, Knaak et al. [33] conducted a research study to investigate the effectiveness of various ML classification methods (KNN, SVM, MLP) as well as different CNN architectures (ResNet, Inception, MobileNetV2). The study aimed to classify six different defect classes and employed a substantial dataset of approximately 14,000 images for training and evaluation.

Meanwhile, addressing porosity issues in laser welding is critical, given the various sizes, shapes, and positions in which these defects are apparent [8], understanding the mechanisms responsible for pore formation is necessary. Conventional techniques for checking post-welding pores, such as cutting or using X-rays, are impractical for manufacturing and time-consuming. However, real-time monitoring of keyhole collapse to prevent subsequent events that may lead to pore formation proves even more demanding and is a highly challenging task [24], [38]. Several influential factors could significantly affect the development process and formation of defects such as porosities and micro-cracks in the welding process. Hence, this requires a deep understanding and analysis of the keyhole's solidification phenomenon during welding to identify porosity regions and understand better and identify the cause of its formation.

Rivera et al. [24] utilized the random forest algorithm, SVM, and ANN to extract features from images and classify weld quality in aluminum alloys. Ma et al. [25] utilized a Deep Belief Network (DBN) to classify the welding areas as either with porosity or non-porosity regions based on the analysis of optical signals. However, due to its complexity, the prediction of pore volume was less accurate than the prediction of welding depth. In another attempt, Zhang et al. [38] demonstrated the capability of Convolutional Neural Networks (CNN) in detecting pores. Their findings revealed that CNN achieved an impressive accuracy rate of 96.1%. However, they also mentioned that detecting deep and tiny pores presents a significant challenge.

Apart from having the previous studies in mind, this paper introduces a DL to predict two KPCs (welding depth and average volume of porosities) with a high accuracy using KICs (geometry, repetition of geometry paths, feed rates for each path, BLW ratio to the core for each path, and other parameters like machine energy output and nozzle usage during welding). The data are derived from numerical hairpin welding experiments, offering deeper insights into the relationship between KICs and these critical KPCs. Unlike [29-33], this paper does not involve the classification of weld quality. Instead, it predicts numerical values for welding depth and average porosity volume using a broader range of KICs, in contrast to the two/three KPCs used in the referenced studies [26-28].

This research aims to develop models that enhance our understanding of the correlation between KPCs and KICs in hairpin welding by exploring DL capabilities. This study represents a key milestone in our ongoing research, which centers on implementing ML concepts to advance online quality assurance processes and techniques for laser welding applications. To establish the essential groundwork, Section 2 clarifies the experimental preparations involving the

preparation of Cu-ETP strips for hairpin welding and delineating laser machine parameters. Subsequently, it explains the dataset derived from

distinct welding configurations, each characterized by specific welding paths and parameters. Furthermore, the approaches utilized to measure these KPCs within the dataset are provided. Specifically, the relationships between various parameters are analyzed using correlation coefficients. In Section 3, the section proceeds to define the particulars of the designed DL model, followed by an evaluation of its performance. In Section 4, The results are thoroughly discussed and evaluated in detail.

2 Data preparation and explanation

2.1 Experiment setup

This study utilized pure enameled copper of Electrolytic Tough Pitch (Cu-ETP) strips with a rectangular cross-section. Before the welding practices, the strips were first cut to a specific length, and approximately 10 mm of insulation was removed from the welding area. Furthermore, the top surface was milled to reduce height deviation and achieve a suitable surface. Particular attention was paid to preventing gaps in the upper part of the welded hairpins. A cross jet was consistently employed to prevent the spatter from reaching the laser lens. A high-pressure air jet safeguards the laser lens against unwanted debris (nozzle) in some samples. The process chain for hairpin stator production is illustrated in Figure 1.

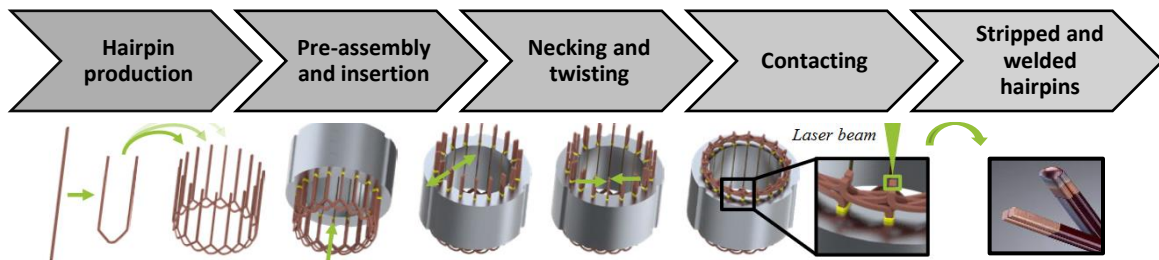


Figure 1 the process chain for hairpin stator production edited from [29].

TRUMPF TruLaser Cell 3000 5-axis laser machine equipped with a TRUMPF TruDisk 6001 laser source boasting a power output capacity of up to 6 kW was utilized for the welding practices. The machine was also equipped with programmable focusing optics (PFO) mounted on the machine's movable portal axis, enabling precise control and positioning of the laser beam during welding operations and ensuring the accuracy and reliability required for repeated experiments. The experiments utilized the innovative Bright Line Weld (BLW) technology

developed by TRUMPF. The core fiber diameter was 100 micrometers and 400 micrometers, respectively. The focal length (L_{foc}) and collimation length (L_{col}) were selected as 255 mm and 150 mm, respectively. The presented technology and set-up facilitated the integration of the inner spot of the laser beam (d_{foc}), which had a diameter of 0.17 mm, with an outer ring having a more significant focus diameter (d_{f-out}) of 0.68 mm.

Using BLW in this experimental set-up, as illustrated in Figure 2, allowed for expanding the keyhole's opening, helping release metal vapor and significantly reducing spatter occurrence [34].

2.2 Input features (KICs)

The data captured and used in the present study was obtained from a series of practical experiments conducted on 12 unique distinct welding geometry configurations. Each geometry involved three different welding paths, wherein a path represents the trajectory followed by the laser beam focal point moving across the workpieces. The current study also examines the various dimensions associated with these pathways. Figure 3 illustrates the first geometry with its three corresponding paths. The first path, P_1 , consisted of multiple iterations arranged in an elliptical shape. The heat from P_1 affected the adjacent piece, increasing the temperature and heating the first pin. Subsequently, P_2 was designated as the second path, executed for the first hairpin, and required multiple repetitions. The molten regions of both workpieces fused, forming a mixed connection. P_1 and P_2 were conducted in opposing directions in certain samples.

The third step, denoted as P_3 , aimed to increase the molten area's size and ensure a metal connection from the first and second pins. Unlike the elliptical shapes employed in P_1 and P_2 ,

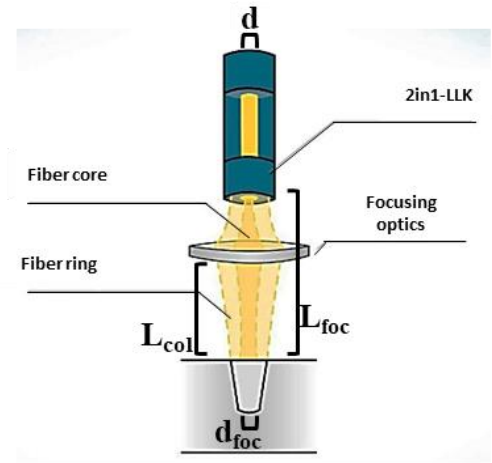


Figure 2 core and ring (BLW) image from [23].

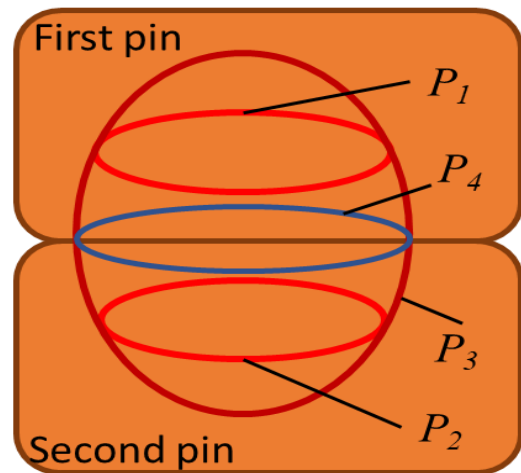


Figure 3 example of the welding path for one of the geometries.

P₃ adopted a nearly circular shape with different repetitions. This choice of a circular shape was motivated by the intention to prevent the formation of "energy hotspots" in the gaps between the metal parts. Rapid movement of the laser beam focal point and pre-existing molten pools from P₁ and P₂ could lead to localized areas of high energy within the gaps, forming a hotspot [34]. In certain geometries, an additional path, denoted as P₄ was investigated in the vicinity of the connection area, yielding encouraging results. The used dataset contained categorical data of the geometrical features, while the geometrical dimensions were not incorporated as inputs in the model. Re-P₁, Re-P₂, Re-P₃, and Re-P₄ were quantitatively represented as numerical data, representing the repetition of each path. The dataset includes information on the total length and duration of all paths for various geometries with different paths. The optimization of the feed rate is typically dependent on the specific material, thickness, and path of the welded joint. Other studies have shown that increasing the feed rate can stabilize the copper and aluminum welding process [10], [35].

For our experiments, the feed rates were also examined for each path at a laser power of up to 6 kW to optimize the welding process. Our dataset includes a feed rate feature for each path and the energy directed toward the core fiber of the laser machine. Due to the initial solid state of copper, a significant amount of energy reflection is expected. Therefore, a greater energy output would result in a more substantial heat input per unit of time. However, in P₃, excessive energy directed towards the core could lead to undesired melting or distortion of the workpiece. The feed rate varied from 150 mm/s to 500 mm/s across four paths. The laser's power intensity distribution in the core fiber and the ring differs between paths in different geometries. The dataset includes BLW ratio core % for paths (P₁-P₃), referred to as features E₁, E₂, and E₃. The range of all weld parameters is listed in Tables 1 and 2.

Table 1

Illustrates the welding parameters applied to the twelve distinct geometries encompassed within the dataset. Determining parameter variations is contingent upon the accumulated expertise and experiential knowledge in conjunction with the employed trial-and-error methodology during the study.

Welding parameter for 12 geometries				
Designation of geometry	P ₁	P ₂	P ₃	P ₄
Number of geometry repetitions	[2-4]	[1-2]	[1-3]	[0-2]
Feed rate [mm/s]	[180-321]	[180-321]	[150-500]	[0-290]
BLW ratio core %	[30-100]	[40-100]	[40-100]	40

Table 2

Welding parameters for the first geometry.

Geometry	Number of repetitions				BLW ratio core % for different paths				The feed rate for the four paths [mm/s]			
	Re-P ₁	Re-P ₂	Re-P ₃	Re-P ₄	E ₁	E ₂	E ₃	E ₄	FR-P ₁	FR-P ₂	FR-P ₃	FR-P ₄
1	3	2	1	0	40	40	40	0	250	250	250	0

2.3 KPCs (model output)

In our used dataset, two KPCs were featured as outputs: (1) Welding depth [mm] and (2) average porosity volume [mm³]. These measurements were obtained using an RX solution computed tomography (CT) scanner. In addition to that, the welding depth was further confirmed in specific samples through a combined metallographic examination. For the CT scan examinations, the welded samples underwent scanning in the CT scanner using a voxel size of 50 μm. The minimum porosity volume was identified as 2×2×2 voxels size. A CT scan was acquired for each welding joint. The average pore volume [mm³] was measured using “VG

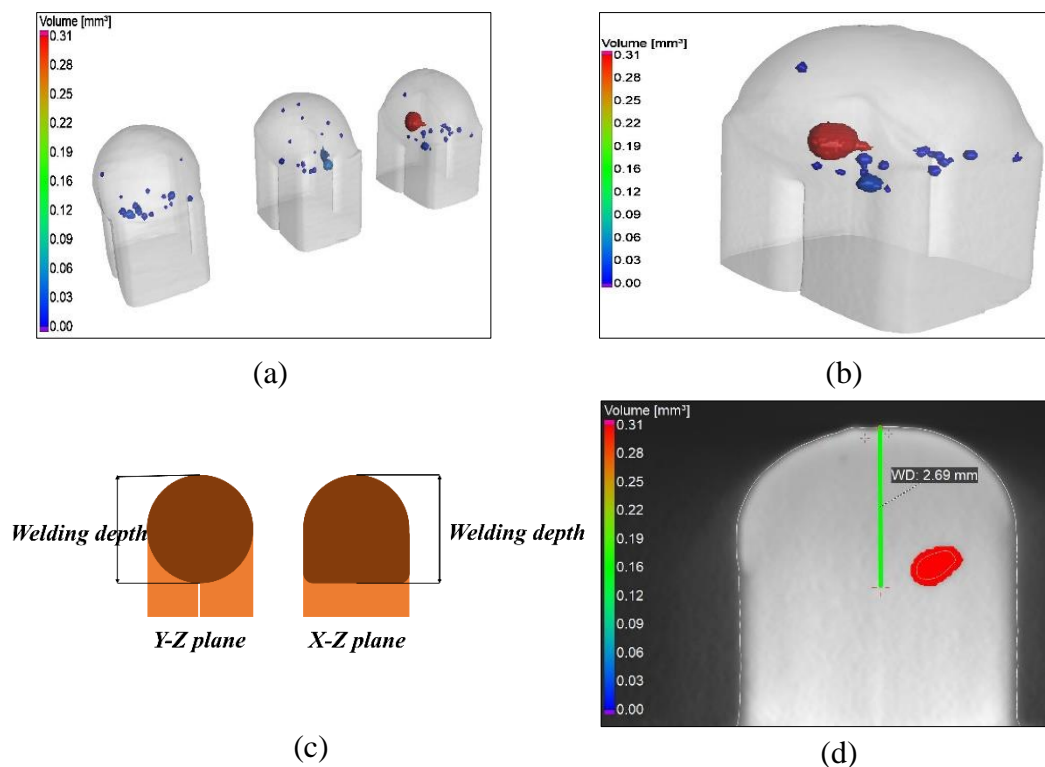


Figure 4 illustrating porosities and welding depth measurements in CT scans Using VG Studio Max Software. (a) volume of porosities for three hairpin samples, with a color bar representing varying porosity volumes, (b) porosity volume within one of the three samples, (c) visual representations of welding depth in hairpins from two perspectives (Y-Z and X-Z), (d) the manual measurement of welding depth using the software, achieved by selecting the endpoint of the depth based on the small gap observed between the two hairpins in the Y-Z view.

Studio Max.” The software mentioned above was utilized to measure the depth of welding manually. Figure 4 shows an example of a measurement of pore volume and welding depth from the CT scan.

2.4 Exploratory Data Analysis

After conducting experiments and measuring the KPCs, the final dataset comprised 134 samples. The preprocessing stage involved converting categorical data through label encoding and data normalization using the sklearn MinMaxScaler in Python. This was followed by a deeper understanding and exploration of the dataset before proceeding with model design.

Investigating the interrelationship between the KICs and KPCs was a key milestone for the present study. A similar attempt by Sinha [36] utilized statistical correlations before applying ML techniques to explain the relationship between welding parameters. One typical reduction of input features for the DL model through correlation analysis was presented by Zhang [37]. The presented correlation coefficients in this research indicate the degree of linear interdependence between variables, which has been determined by calculating covariance. This computation reveals the directional relationship within variables. A positive covariance indicates synchronized movements, whereas a negative covariance shows opposing movements [37].

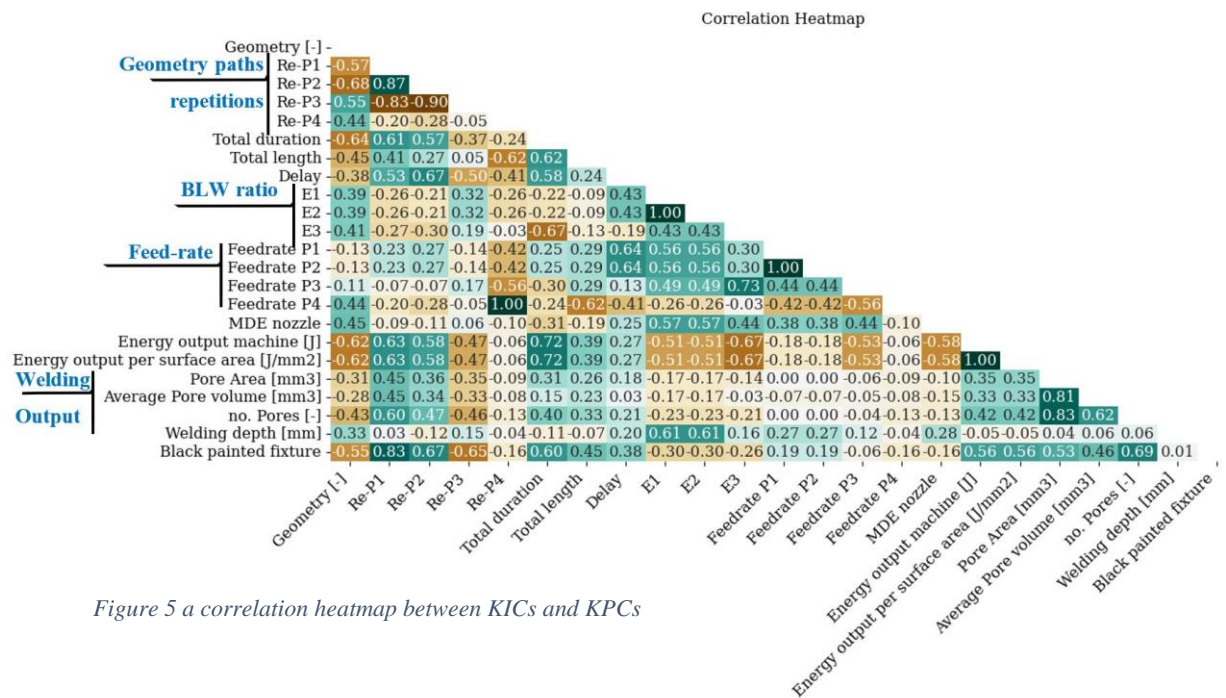


Figure 5 a correlation heatmap between KICs and KPCs

The data analysis examined the correlation between the KICs and the KPCs (welding depth and average pore volume). The results were presented in Python using Seaborn heatmaps, as illustrated in Figure 5. The heatmap correlation revealed a significant correlation between variables BLW ratio for the first and second paths (E_1 , E_2) and the welding depth. Furthermore, the performed analysis indicated that E_1 and E_2 are the two parameters that mainly determine and affect the welding depth to approximately 60%, as shown in the correlation heatmap. Consequently, higher values for (E_1 and E_2) increased the welding depth. Moreover, a weak correlation was observed between the number of repetitions for the first path and the welding depth. This could be attributed to the welding depth not being significantly influenced or governed during this initial material heating stage [7].

Besides, weak correlations were identified between the number of repetitions for paths two and three ($Re-P_2$, $Re-P_3$) and the welding depth. Furthermore, it was noticeable that $Re-P_4$ did not significantly affect the welding depth, as the repetitions ($Re-P_2$, $Re-P_3$) already determine its formation. Furthermore, a strong positive correlation was observed between the pore volume/number of pores and path repetitions. It was also noted that an increase in $Re-P_3$ led to decreased pore volume/number of pores.

2.5 Distribution

Understanding the level of stochasticity in the output variables aided in selecting suitable algorithms. Additionally, it enabled the development of a deep learning model capable of capturing and generalizing the underlying patterns in the data. This preliminary analysis aimed to assess whether the variables intended for prediction demonstrate increased levels of stochasticity. Displaying the distribution of the outputs could give an insight into the variability and patterns exhibited by output variables. Figure 6 (a) demonstrates the welding depth variable similar to a normal distribution. A variable that follows a normal distribution indicates a well-behaved linear model, suggesting a higher level of predictability within the dataset.

As Liu et al. claimed in their study [27], the porosity number and its distribution were influenced not by a single welding parameter but rather by a complex interaction of multiple welding parameters. Figure 6 (b) illustrates the distribution of the average pore volume within the dataset and the extent of deviation from the normal distribution.

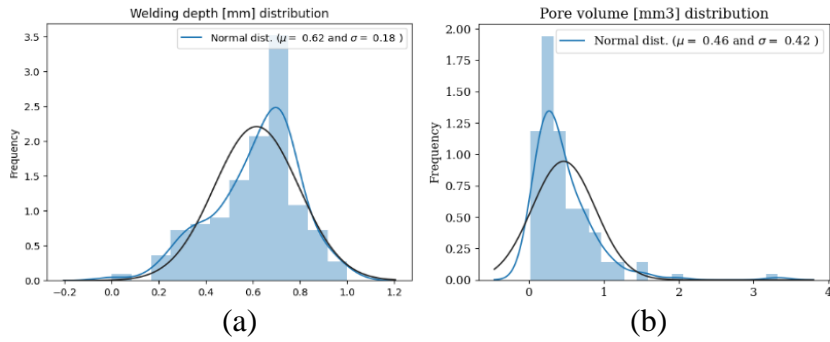


Figure 6 displays the distribution of the output variables overlaid in black on the histogram of the respective data variables. (a) illustrates the distribution of the first output variable (welding depth), (b) the distribution of the second output (pore volume).

3 Methodology

3.1 Design 2 DL networks to estimate the two of the KPCs (welding depth and average pore volume)

The present study aims to employ a DL model to predict the depth of the laser welding. The dataset consists of 20 distinct features, and there is a total of 134 samples available for analysis. The dataset was partitioned into a training set comprising 80% of the data and a validation set comprising 10% of the data. The remaining 10% of the dataset was allocated for the test dataset.

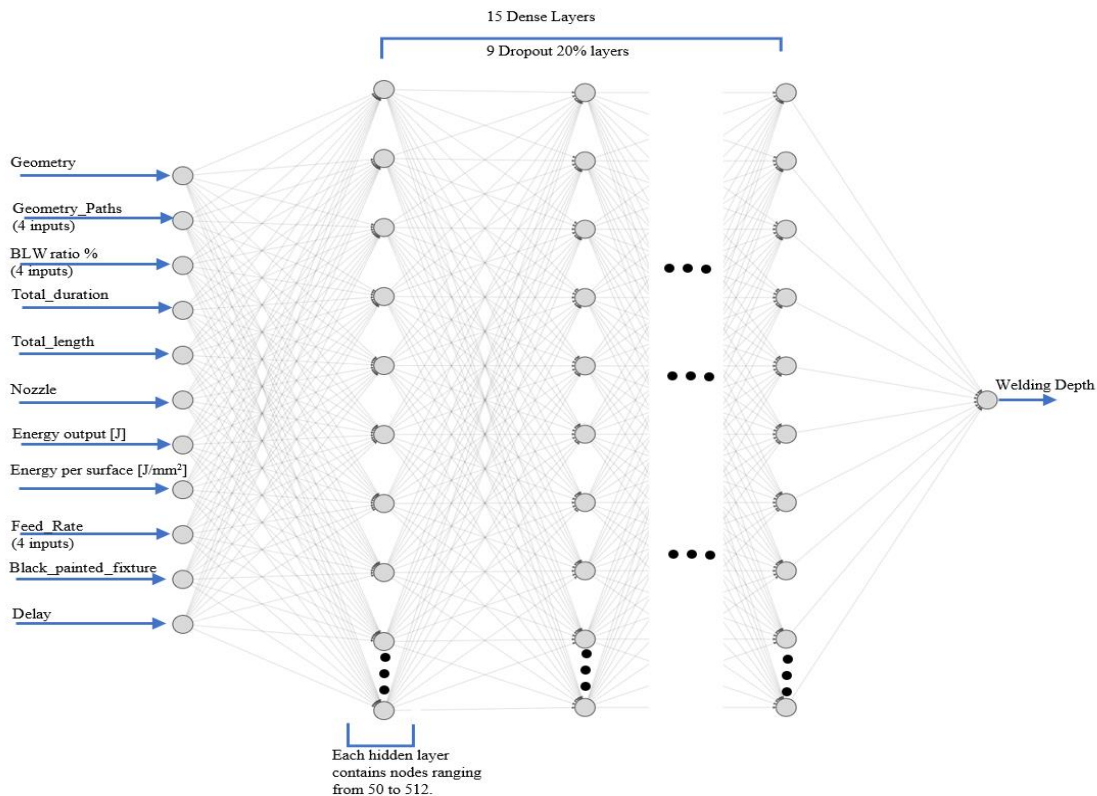


Figure 7 deep learning architecture for welding depth prediction. Average pore volume prediction uses a very similar DL architecture.

Various DL models (wide, wide-deep, deep) were tested to examine the optimal architecture for the neural network. To evaluate the efficiency of the model, three statistical metrics were computed. Firstly, the loss function was calculated for both the training and validation epochs. The loss function quantified the discrepancy between predicted and actual values. Decreased loss signified superior performance and a stronger correlation between the predicted and actual values. In our presented models, the Mean Squared Logarithmic Error (MSLE) was used as the loss function to provide the benefit of penalizing underestimations more heavily than overestimations. This choice addressed situations where underestimating specific values can result in more significant repercussions. Concurrently, the Mean Absolute Error (MAE) was used as a statistical metric to assess the model's performance. It quantified the average absolute difference between the predicted and actual values. The MAE provides a straightforward evaluation of the model's precision. The coefficient of determination (R^2) is employed as an evaluation metric to measure overfitting in the model. A key aspect is assessing the proportion of variance in the dependent variable that can be predicted from the independent variables. Including R^2 as an evaluation metric enables examining the model's capacity beyond the training dataset.

A model utilizing a linear activation function and Adam optimizer function, employing a default learning rate, to predict welding depth. Following this, a model tuning process was executed, involving exploring various parameters, including the number of hidden layers, the neuron count within each layer, the optimizer, and the learning rate. The resulting model comprises 15 dense layers, with its architectural representation in Figure 7. The training phase encompassed 1,000 epochs, with a consistent batch size of 32 samples.

This work employs a similar DL model to predict pore volume. Also, after tuning the model best result is achieved with six dense layers, and the last dense layer utilizes a linear activation function. The optimizer function used was Adam. The model was trained for one thousand epochs, utilizing a batch size of 32 samples. A distinct subset of the dataset, comprising 10% of the original dataset, was used to predict welding depth.

4 Results and discussion

The learning curve shown in Figure 8 provides a comprehensive representation of the DL model's performance throughout the training and validation epochs. In this context, the learning

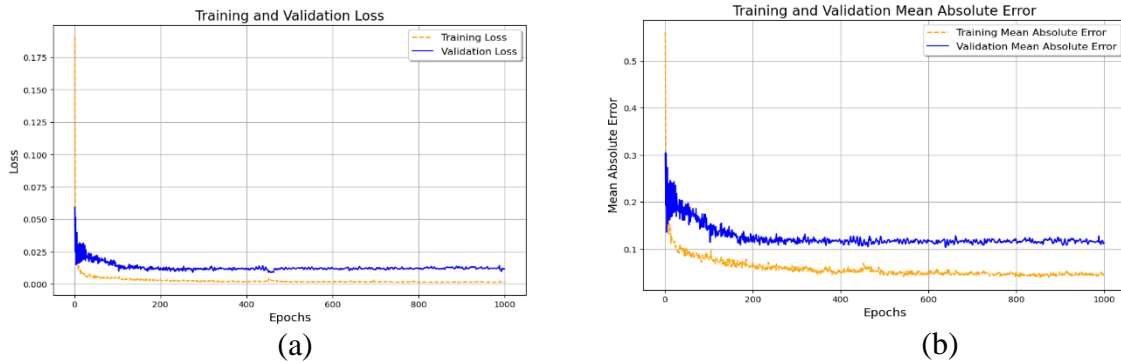


Figure 8 displays the learning curve of the welding depth prediction network represented by two lines: orange for the training phase and blue for the validation phase. In (a), the narrow curves illustrating loss values over 1000 epochs for both training and validation datasets indicate reasonable model generalization. In (b), the slight gap observed between the curves of MAE values over 1000 epochs suggests the model's struggle to avoid overfitting in the validation dataset.

curve signifies the dynamic evolution of the model's predictive ability to make predictions as it acquires knowledge from the training data and generalizes to unseen data.

Loss is a fundamental metric that quantifies the difference between the predicted welding depth and ground truth values. As seen in Figure 8, a decreasing orange line indicates that the model successfully reduces discrepancies and effectively minimizes errors between the predicted and the actual data during the training phase. This suggests that the model is acquiring the ability to comprehend and learn to capture the underlying patterns within the training data. It converges toward a state where its predictions closely align with the actual values. The meeting of the curves signifies that the model is effectively learning and generalizing from the training data, leading to accurate predictions of welding depth values on new, unseen data in the validation phase. This finding demonstrates the model's proficiency in capturing intricate connections and making reliable predictions in estimating the welding depth.

A loss value **0.0111** shows that the model's predicted welding depth slightly deviates from the actual value. The model has successfully acquired the ability to estimate welding depth during the validation phase accurately. Similarly, a MAE value of **0.1079** shows that the model's predictions for welding depth have a minimal average absolute difference from the actual value. The small MAE value indicated that the model effectively minimizes errors and provides accurate predictions for welding depth.

As seen in Figure 9 the model's predictions of welding depths were subsequently matched against the actual welding depths in the real dataset. This evaluation aimed to assess the precision and efficiency of the trained model in capturing and reproducing the inherent patterns and trends within the welding procedure. The model's predictive capability is determined by comparing its predictions to the actual welding depths. A stronger correspondence between the predicted and actual welding depths showed a more dependable and accurate model, see Figure 9.

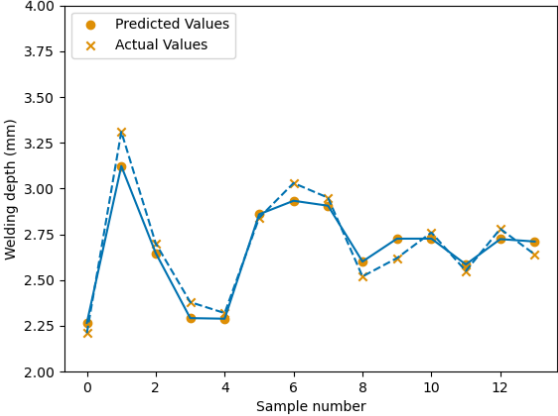


Figure 9 shows the predicted welding depth in the test dataset, compared with the actual values.

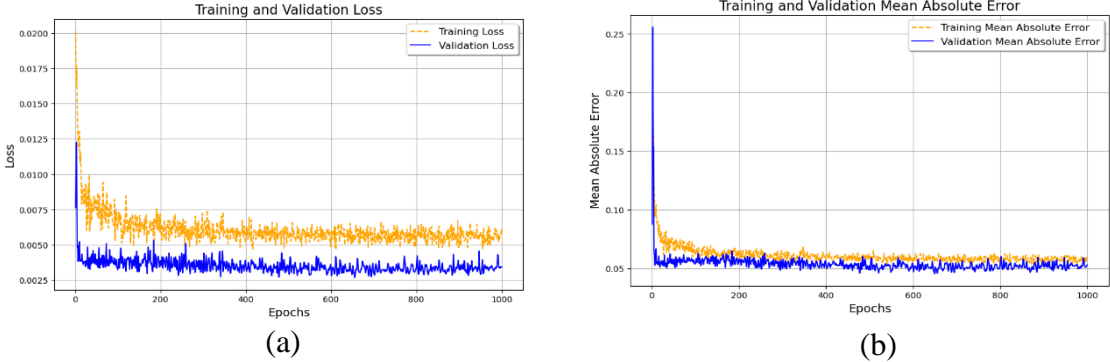


Figure 10 displays the learning curve represented by two lines: orange for the training phase and blue for the validation phase. In (a), it shows loss values over 1000 epochs, while (b) illustrates MAE values over the same epochs. The lower position of the validation curve compared to the training curve might indicate underfitting.

Figure 10 illustrates the learning curves for predicting average pore volume. The subsequent validation dataset displayed a loss metric of **0.0067** and a (MAE) of **0.0641**. The validation curve positioned lower than the training curve suggests possible underfitting. Consequently, the calculated R^2 value of **0.2095** highlights the model's limited ability to explain variance in the validation data. Illustrating the model's challenges in accurately capturing the variance present

in the data. The results from the comparison between the predicted values in the test dataset and actual data are shown in Figure 11.

5 Conclusion

This study come with a robust DL model and development that could predict two critical welding KPCs (welding depth and average pore volume). This

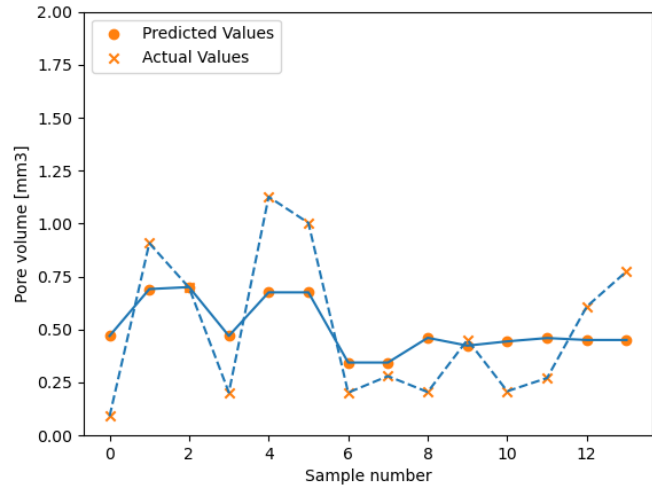


Figure 11 predicted pore volume in the test dataset.

achievement was not just based on numerical data but also on the extensive experiments conducted as a fundamental part of this research. In addition to that, the developed DL model considered a full array of KICs, including geometric factors, path geometries, repetitions, feed rates, BLW ratio, machine energy output, and a welding nozzle, which significantly affected the quality of the final welds. Develop a model to capture the complex interactions between the input variables, resulting in a model offering high fitting accuracy. Following the fine-tuning, the model achieved **0.1079** for MAE in the validation dataset in predicting welding depth and **0.0641** for MAE in predicting the average volume of porosities.

In conclusion, this experimental and statistical research work could be a good foundation for our ongoing research studies. However, further investigations are going to be conducted involving combining additional data from various sources, including generated data, simulation data, and sensor data, to enhance weld quality and push even more the accuracy and reliability of the presented model. There is great interest and demand to achieve a robust and optimized online quality assurance system that utilizes DL to predict KPCs and autonomously optimize KICs in real-time welding processes.

6 Conflict of Interests

The authors declare no conflicts of interest.

7 Acknowledgment

Vinnova is greatly appreciated for funding this work through Production 2030 programme, grant number 2021-03693. Formas and the Swedish Energy Agency are appreciated for their valuable support and collaboration. Volvo Cars as a valued partner to our research works, is sincerely appreciated, for their continues support and materials.

References

1. 2030 Climate Target Plan. [cited 2023 31-07]; Available from: https://climate.ec.europa.eu/eu-action/european-green-deal/2030-climate-target-plan_en.
2. Palka, R. and M. Wardach, Design and Application of Electrical Machines. 2022, MDPI. p. 523. <https://doi.org/10.3390/en15020523>
3. Mao, Y., et al., A deep learning framework for layer-wise porosity prediction in metal powder bed fusion using thermal signatures. *Journal of Intelligent Manufacturing*, 2023. 34(1): p. 315-329. <https://doi.org/10.1007/s10845-022-02039-3>
4. Selema, A., M.N. Ibrahim, and P. Sergeant, Electrical machines winding technology: Latest advancements for transportation Electrification. *Machines*, 2022. 10(7): p. 563. <https://doi.org/10.3390/machines10070563>
5. Soltani, M., et al. Considerations on the preliminary sizing of electrical machines with hairpin windings. in 2021 IEEE Workshop on Electrical Machines Design, Control and Diagnosis (WEMDCD). 2021. IEEE. <https://doi.org/10.1109/WEMDCD51469.2021.9425645>
6. Tobias Glaessel, D.B.P., Michael Masuch, Dieter Gerling, Joerg Franke, Manufacturing Influences on the Motor Performance of Traction Drives with Hairpin Winding. *IEEE Xplore*. <https://doi.org/10.1109/EDPC48408.2019.9011872>
7. Dimatteo, V., et al., The effect of process parameters on the morphology, mechanical strength and electrical resistance of CW laser-welded pure copper hairpins. *Journal of Manufacturing Processes*, 2021. 62: p. 450-457. <https://doi.org/10.1016/j.jmapro.2020.12.018>
8. Berger, P., H. Hügel, and T. Graf, Understanding Pore Formation in Laser Beam Welding. *Physics Procedia*, 2011. 12: p. 241-247. <https://doi.org/10.1016/j.phpro.2011.03.031>
9. Farrokhi, F., B. Endelt, and M. Kristiansen, A numerical model for full and partial penetration hybrid laser welding of thick-section steels. *Optics & Laser Technology*, 2019. 111: p. 671-686. <https://doi.org/10.1016/j.optlastec.2018.08.059>
10. Shen, J.J., H.J. Liu, and F. Cui, Effect of welding speed on microstructure and mechanical properties of friction stir welded copper. *Materials & Design*, 2010. 31(8): p. 3937-3942. <https://doi.org/10.1016/j.matdes.2010.03.027>
11. Amanat, N., et al., Transmission laser welding of amorphous and semi-crystalline poly-ether-ether-ketone for applications in the medical device industry. *Materials & design*, 2010. 31(10): p. 4823-4830. <https://doi.org/10.1016/j.matdes.2010.04.051>
12. Acherjee, B., Laser transmission welding of polymers—a review on welding parameters, quality attributes, process monitoring, and applications. *Journal of Manufacturing Processes*, 2021. 64: p. 421-443. <https://doi.org/10.1016/j.jmapro.2021.01.022>

13. Cai, W., et al., *Application of sensing techniques and artificial intelligence-based methods to laser welding real-time monitoring: A critical review of recent literature.* Journal of Manufacturing Systems, 2020. 57: p. 1-18. <https://doi.org/10.1016/j.jmsy.2020.07.021>
14. Wu, D., et al., Progress and perspectives of in-situ optical monitoring in laser beam welding: Sensing, characterization and modeling. Journal of Manufacturing Processes, 2022. 75: p. 767-791. <https://doi.org/10.1016/j.jmapro.2022.01.044>
15. Chen, Z., et al., Journal of Manufacturing Processes, 2018. 31: p. 1-8. Numerical and experimental investigation on laser transmission welding of fiberglass-doped PP and ABS. <https://doi.org/10.1016/j.jmapro.2017.10.013>
16. Ge, W., J.Y. Fuh, and S.J. Na, Numerical modelling of keyhole formation in selective laser melting of Ti6Al4V. Journal of Manufacturing Processes, 2021. 62: p. 646-654. <https://doi.org/10.1016/j.jmapro.2021.01.005>
17. Jiang, M., et al., Numerical study of thermal fluid dynamics and solidification characteristics during continuous wave and pulsed wave laser welding. International Journal of Thermal Sciences, 2022. 181: p. 107778. <https://doi.org/10.1016/j.ijthermalsci.2022.107778>
18. Jia, H., et al., Numerical simulation and experiment for the dynamic behavior of molten pool in ultrasonic-assisted MIG welding. International Journal of Heat and Mass Transfer, 2023. 215: p. 124469. <https://doi.org/10.1016/j.ijheatmasstransfer.2023.124469>
19. Li, J., et al., Numerical and experimental study on keyhole dynamics and pore formation mechanisms during adjustable-ring-mode laser welding of medium-thick aluminum alloy. International Journal of Heat and Mass Transfer, 2023. 214: p. 124443. <https://doi.org/10.1016/j.ijheatmasstransfer.2023.124443>
20. Zhang, H., et al., Numerical and experimental investigation of the formation mechanism and the distribution of the welding residual stress induced by the hybrid laser arc welding of AH36 steel in a butt joint configuration. Journal of Manufacturing Processes, 2020. 51: p. 95-108. <https://doi.org/10.1016/j.jmapro.2020.01.008>
21. Chu, H., et al., Multi-physics multi-scale simulation of unique equiaxed-to-columnar-to-equiaxed transition during the whole solidification process of Al-Li alloy laser welding. Journal of Materials Science & Technology, 2023. <https://doi.org/10.1016/j.jmst.2023.05.077>
22. Jiang, P., et al., Multi-physics multi-scale simulation of the solidification process in the molten pool during laser welding of aluminum alloys. International Journal of Heat and Mass Transfer, 2020. 161: p. 120316. <https://doi.org/10.1016/j.ijheatmasstransfer.2020.120316>
23. Low-Spatter Welding with Beam Formation Technology | TRUMPF. [cited 2023 June]; Available from: https://www.trumpf.com/en_IN/solutions/applications/laser-welding/low-spatter-welding-with-beam-formation-technology.
24. Rivera, J. S., Gagné, M. O., Tu, S., Barka, N., Nadeau, F., & Ouafi, A. E. (2023). Quality classification model with machine learning for porosity prediction in laser welding aluminum alloys. Journal of Laser Applications, 35(2). <https://doi.org/10.2351/7.0000769>
25. Ma, D., et al., Online porosity prediction in laser welding of aluminum alloys based on a multi-fidelity deep learning framework. Journal of Intelligent Manufacturing, 2022. <https://doi.org/10.1007/s10845-022-02033-9>
26. Yusof, M., M. Ishak, and M. Ghazali, Weld depth estimation during pulse mode laser welding process by the analysis of the acquired sound using feature extraction analysis

- and artificial neural network. *Journal of Manufacturing Processes*, 2021. 63: p. 163-178. <https://doi.org/10.1016/j.jmapro.2020.04.004>
27. Liu, B., et al., Optimal design for dual laser beam butt welding process parameter using artificial neural networks and genetic algorithm for SUS316L austenitic stainless steel. *Optics & Laser Technology*, 2020. 125: p. 106027. <https://doi.org/10.1016/j.optlastec.2019.106027>
 28. Luo, M. and Y.C. Shin, Estimation of keyhole geometry and prediction of welding defects during laser welding based on a vision system and a radial basis function neural network. *The International Journal of Advanced Manufacturing Technology*, 2015. 81(1-4): p. 263-276. <https://doi.org/10.1007/s00170-015-7079-1>
 29. Mayr, A., J. Bauer, and J. Franke, A multi-view deep learning approach for quality assessment in laser welding of hairpin windings based on 2D image captures. *Procedia CIRP*, 2022. 115: p. 196-201. <https://doi.org/10.1016/j.procir.2022.10.073>
 30. Zhao, X., et al., Analysis of dynamic characteristics of vapor plume of oscillating laser welding of SUS301L-HT stainless steel. *Optics & Laser Technology*, 2023. 159: p. 108947. <https://doi.org/10.1016/j.optlastec.2022.108947>
 31. Hartung, J., et al., Camera-Based In-Process Quality Measurement of Hairpin Welding. *Applied Sciences*, 2021. 11(21): p. 10375. <https://doi.org/10.3390/app112110375>
 32. Shin, J., Kang, S., Kim, C., Hong, S., & Kang, M. (2023). Identification of solidification cracking using multiple sensors and deep learning in laser overlap welded Al 6000 alloy. *Journal of Laser Applications*, 35(4). <https://doi.org/10.2351/7.0001112>
 33. Knaak, C., et al., Deep Learning and Conventional Machine Learning for Image-Based in-Situ Fault Detection During Laser Welding: A Comparative Study. 2021, ENGINEERING. <https://doi.org/10.20944/preprints202105.0272.v1>
 34. Omlor, M., et al., Quality characteristics and analysis of input parameters on laser beam welding of hairpin windings in electric drives. *Welding in the World*, 2023. <https://doi.org/10.1007/s40194-023-01500-y>
 35. Fetzer, F., et al., Geometry and stability of the capillary during deep-penetration laser welding of AlMgSi at high feed rates. *Optics & Laser Technology*, 2021. 133: p. 106562. <https://doi.org/10.1016/j.optlastec.2020.106562>
 36. Sinha, A.K., D.Y. Kim, and D. Ceglarek, Correlation analysis of the variation of weld seam and tensile strength in laser welding of galvanized steel. *Optics and lasers in engineering*, 2013. 51(10): p. 1143-1152. <https://doi.org/10.1016/j.optlaseng.2013.04.012>
 37. Zhang, Y., X. Gao, and S. Katayama, Weld appearance prediction with BP neural network improved by genetic algorithm during disk laser welding. *Journal of Manufacturing Systems*, 2015. 34: p. 53-59. <https://doi.org/10.1016/j.jmsy.2014.10.005>
 38. Zhang, B., K.-M. Hong, and Y.C. Shin, Deep-learning-based porosity monitoring of laser welding process. *Manufacturing Letters*, 2020. 23: p. 62-66. <https://doi.org/10.1016/j.mfglet.2020.01.001>